Modelling Ignition, Combustion, and Pollutant Emissions

12

Pooria Farmand and Heinz Pitsch

Contents

Abstract

In this chapter, the ignition, combustion, and pollutant formation of solid fuel particles under different operating conditions are investigated using detailed numerical

---

P. Farmand (✉) · H. Pitsch
Institute for Combustion Technology, RWTH Aachen University, Aachen, Germany
e-mail: p.farmand@itv.rwth-aachen.de

H. Pitsch
e-mail: h.pitsch@itv.rwth-aachen.de

R. Kneer et al. (eds.), *Clean Energy Conversion*,
https://doi.org/10.1007/978-3-031-98956-8_12

simulations. First, coal and biomass combustion in a laminar flow reactor configuration are compared, showcasing similar combustion characteristics between coal and biomass. Then, particle/particle interaction effects in the particle group configuration are investigated, indicating later ignition time and flame opening behaviour in higher particle number densities. Particle/chemistry/turbulence interactions are also studied in particle cloud combustion under isotropic turbulence, where ignition is found to occur most likely outside of particle clusters. To assess the reduced-order flamelet models for solid fuel combustion, the optimal estimator concept is employed using the generated dataset, revealing that modelling errors increase near particles. Finally, NO_x formation during solid fuel combustion is analysed. The highest NO_x formation is found to occur near the particle groups around stoichiometric mixtures. Important pathways for NO_x formation under different operating conditions are studied, revealing the dominance of the fuel-NO_x pathways.

12.1 Introduction

The advantages of numerical methods for improving solid fuel combustion systems are still not used to their full potential. Direct numerical simulation (DNS) is an established tool to study fundamental aspects of combustion. However, due to the complexities associated with biomass combustion, DNS requires various submodels for the biomass's thermo-chemical conversion. Solid fuel combustion can be simulated via particle-resolved or point-particle approaches. Due to several challenges and limitations of reactive simulations with a particle-resolved approach, solid fuel combustion has been investigated mostly by means of point-particle approaches in the Euler-Lagrange framework. Since such simulations cannot resolve the immediate surroundings of the particle, the interactions of flow and particle are typically described by so-called film models. In these models, all relevant features, such as the typical geometrical characteristics and the internal structure of the solid particles, should be considered. Appropriate model formulations can be derived from experimental results or simplified resolved simulations.

The overarching goal of developing this type of numerical framework is to enable the investigation of ignition, combustion, and pollutant formation of solid fuels under various conditions. The correct prediction of the combustion characteristics of solid fuels involves many factors. Fuel type, particle geometry and internal structure, and the operating conditions of the burner significantly affect the combustion characteristics and pollutant formation pathways in solid fuels. The inclusion of detailed submodels in the point-particle framework is crucial for predicting the correct physical behaviour for ignition and combustion, which can be validated based on experimental data. By resolving the Eulerian field and using detailed kinetics, point-particle DNS can provide data that are otherwise inaccessible in experiments. These data can serve as a reference guideline for the development of the reduced order models required for large-scale simulations, highlighting the value and innovation of this research.

In this chapter, a point-particle direct numerical simulation framework is employed to study the ignition, combustion, and NO_x formation of single particles and groups of coal and biomass particles under laminar and turbulent conditions. In Sect. 12.2, the relevant models and methods for the point-particle DNS in the fully coupled Euler-Lagrange framework are described. Then, in Sect. 12.3, the ignition and combustion of single particle and particle groups are investigated. To investigate the particle/chemistry/turbulence interactions, ignition and combustion modelling for clustering particle clouds in turbulent conditions is presented in Sect. 12.4, in which the PP-DNS dataset is also used for a priori model assessment of the flamelet progress variable (FPV) models. Finally, in Sect. 12.5, the NO_x formation pathways are studied during ignition and combustion of solid fuels.

12.2 Numerical Framework and Modelling

As mentioned in Sect. 12.1, mass, momentum, and energy transfers between a solid particle and its surrounding gas can be either particle-resolved or modelled by a point-particle approximation or a so-called Euler-Lagrange approach, as shown schematically in Fig. 12.1. In the particle-resolved approach, the particle-gas interface and the boundary layer are chemically and spatially resolved. The particle-resolved approach requires computational cells with a size Δx much smaller than the particle diameter D_p. On the other hand, in the point-particle approach, particles are tracked as Lagrangian points, in which $\Delta x \geq D_p$, and the mass, momentum, and energy exchange between the gas phase and particles corresponds to source terms in the conservation equations.

Since the combustion of solid fuels is a multiphase process, gas phase, solid phase, and the interface between the solid and gas phases should be modelled to capture the correct physical behaviour of the particles in the reactive environment. In the following sections, the modelling framework for each of these parts will be presented using the point-particle approach, which is the most used modelling approach for solid fuel combustion.

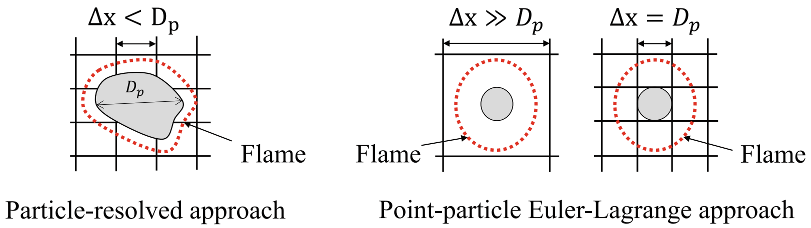

Fig. 12.1 Schematics of the particle-resolved and Euler-Lagrange approaches

12.2.1 Gas-Phase Modelling

Conservation of mass, species, momentum, and energy in the gas phase within the low-Mach formulation leads to the governing equations similar to those applied by Attili et al. [1] as

$$\frac{\partial \rho_{\mathrm{g}}}{\partial t} + \frac{\partial}{\partial x_\beta}\left(\rho_{\mathrm{g}}\, U_{\mathrm{g},\beta}\right) = \dot{S}_m, \tag{12.1}$$

$$\frac{\partial(\rho_{\mathrm{g}}\, Y_i)}{\partial t} + \frac{\partial}{\partial x_\beta}\left(\rho_{\mathrm{g}}\left(U_{g,\beta} + V_{\beta,i}\right) Y_i\right) = \omega_i + \dot{S}_{Y_i}, \tag{12.2}$$

$$\frac{\partial(\rho_{\mathrm{g}} U_{g,\alpha})}{\partial t} + \frac{\partial}{\partial x_\beta}\left(\rho_{\mathrm{g}}\, U_{g,\alpha}\, U_{g,\beta}\right) = -\frac{\partial \Pi}{\partial x_\alpha} + \frac{\partial \tau_{\alpha\beta}}{\partial x_\beta} + \dot{S}_{U,\alpha}, \tag{12.3}$$

$$\begin{aligned} c_{p,\mathrm{g}}\frac{\partial(\rho_{\mathrm{g}}\, T_{\mathrm{g}})}{\partial t} + c_{p,\mathrm{g}}\frac{\partial}{\partial x_\beta}\left(\rho_{\mathrm{g}}\, U_{g,\beta}\, T_{\mathrm{g}}\right) &= -\rho_{\mathrm{g}}\frac{\partial T_{\mathrm{g}}}{\partial x_\beta}\sum_{i}^{N_{\mathrm{s}}} c_{p,g,i}\, Y_i\, V_{\beta,i} \\ &\quad + \frac{\partial}{\partial x_\beta}\left(\lambda_{\mathrm{g}}\frac{\partial T_{\mathrm{g}}}{\partial x_\beta}\right) + \dot{Q}_{\mathrm{g}} + \dot{S}_T. \end{aligned} \tag{12.4}$$

Detailed information on (12.1)–(12.4) can be found the study by Farazi et al. [2]. It should be noted that in (12.1)–(12.4), $\dot{S}_i$ are the source terms from the dispersed phase per unit volume, for which the physical models are described in Sect. 12.2.3. Also, $\dot{Q}_{\mathrm{g}}$ accounts for the rate of heat released per unit volume from the homogeneous reactions in the gas phase. Gas-phase chemistry is modelled using finite-rate chemistry, adopting a specially designed mechanism validated for the oxidation of coal and biomass in both air and oxy-fuel atmospheres. The details of the gas-phase chemical kinetic models can be found in Cai et al. [3] for coal and Chap. 6 for biomass combustion.

12.2.2 Solid-Phase Modelling

In the point-particle approximation, the solid fuel combustion is modelled with a collection of point-particles within the Lagrangian framework by solving (12.5)–(12.8) for trajectory, velocity, mass, and temperature as described by Farazi et al. [2].

The Lagrangian equations are given as

$$\frac{dx^k_{\mathrm{p},\alpha}}{dt} = U^k_{\mathrm{p},\alpha}, \tag{12.5}$$

$$\frac{dU^k_{\mathrm{p},\alpha}}{dt} = f^k_\mathrm{d} \, \frac{18\,\mu_\mathrm{g}\left(U_{\mathrm{g},\alpha} - U^k_{\mathrm{p},\alpha}\right)}{\rho_\mathrm{g}\left(D^k_\mathrm{p}\right)^2}, \tag{12.6}$$

$$\frac{dm^k_\mathrm{p}}{dt} = \dot{m}^k_{\mathrm{p,evap}} + \dot{m}^k_{\mathrm{p,dev}}, \tag{12.7}$$

$$c^k_{p,\mathrm{p}}\, m^k_\mathrm{p} \, \frac{dT^k_p}{dt} = \dot{m}^k_{\mathrm{p,evap}} \Delta H_\mathrm{e} + \dot{m}^k_{\mathrm{p,dev}} \Delta H_\mathrm{d} + \Psi^k_{\mathrm{p,c}} + \Psi^k_{\mathrm{p,r}}, \tag{12.8}$$

where for the k^{th} particle, m^k_p is the total particle mass and D^k_p its diameter. The term $x^k_{\mathrm{p},\alpha}$ refers to the particle position and $U^k_{\mathrm{p},\alpha}$ to the velocity along the α direction. In (12.6), f^k_d is the correction coefficient which accounts for the effect of the Stefan flow on the drag force, which can be computed based on the empirical correlation by Miller and Bellan [4]. Equation (12.8) describes the change of particle temperature assuming a homogeneous temperature inside the particle, which is derived from balancing the heat transfer on the particle surface and the change of thermal energy. Here, the first and second terms on the right hand side refer to the required energy for the evaporation and devolatilisation processes. The heat of evaporation is expressed as ΔH_e and ΔH_d is the heat of devolatilisation. The term $\psi^k_{\mathrm{p,c}}$, accounts for the energy transfer by convection and conduction between the particle and the surrounding gas, while the term $\psi^k_{\mathrm{p,r}}$, accounts for the energy transfer due to radiation. Detailed information on these (12.5)–(12.8) can be found in the studies by Farazi et al. [2,5]. Additionally, various submodels are required to capture the full conversion process of the solid particles. The solid kinetic model, which describes the solid fuel's thermal decomposition, provides information on the mass release rate from the particle, alongside the composition of the released gaseous matter, such as light gases and heavy tars, and the thermal effect of this process on the solid particle during the thermal decomposition process. For the reactive simulations of solid particles in the following sections, different solid kinetic models such as single first-order reaction (SFOR), competing two-step model (C2SM), chemical percolation devolatilisation (CPD), and CRECK-S are used, and the detailed description of these models can be found in Chap. 8.

12.2.3 Solid-Gas Interface Coupling

In order to predict the correct physical behaviour of solid fuel during ignition and combustion, the particle and gas phases should be fully coupled. Therefore, the exchange of species, mass, and energy between the solid phase and the surrounding gaseous region at the solid-gas interface should be considered using a coupling method. In the point-particle approach, the gas phase and the solid phase are fully coupled using the two-way coupling approach through the source terms appearing in the governing equations at each computational cell with volume Ω_g. In the Eulerian-Lagrangian framework, (12.5)–(12.8) are derived according to the film model, assuming a uniform gas field around the particle. To capture the gas-phase ignition, the domain size is discretised with cubic cells of length dx, which is typically equal to the diameter of the mono-disperse particles [2,5]. Since using the gas phase quantities from grid cells with the same size as the particles is not consistent with the film model assumption, a filter should be applied to provide a smoother field in the gas phase to evaluate the state of the gas surrounding the particle consistently with the film model. This approach has been proposed and validated by Farazi et al. [2]. Also, to avoid large particle source terms caused by the small cell-to-particle ratios and to provide grid-independent values, the distribution coefficient ϕ^k for each particle k is adopted [2,5]. The distribution coefficient is computed by a Gauss function with a characteristic width L_d, centred at the k^th particle position. Then, the source terms $\dot{S}_\mathrm{i}$ in the Eulerian equations (12.1)–(12.4) can be written as

$$\dot{S}_m = -\frac{1}{\Omega_\mathrm{g}} \sum_{k=1}^{n_\mathrm{p}} \phi^k \left(\frac{dm_\mathrm{p}^k}{dt} \right) \tag{12.9}$$

$$\dot{S}_{U,\beta} = -\frac{1}{\Omega_\mathrm{g}} \sum_{k=1}^{n_\mathrm{p}} \phi^k \left(\frac{dm_\mathrm{p}^k}{dt} U_{\mathrm{p},\beta}^k + m_\mathrm{p}^k \frac{dU_{\mathrm{p},\beta}^k}{dt} \right) \tag{12.10}$$

$$\dot{S}_{Y_i} = -\frac{1}{\Omega_\mathrm{g}} \sum_{k=1}^{n_\mathrm{p}} \phi^k \left(\frac{dm_{\mathrm{p,dev},i}^k}{dt} \right) \tag{12.11}$$

$$\dot{S}_T = -\frac{1}{\Omega_\mathrm{g}} \sum_{k=1}^{n_\mathrm{p}} \phi^k \left(\frac{dm_\mathrm{p}^k}{dt} c_{p,\mathrm{p}}^k T_\mathrm{p}^k + \dot{\Psi}_{\mathrm{p,c}}^k \right) \tag{12.12}$$

12.3 Modelling Ignition and Combustion of Solid Fuels Under Laminar Conditions

Based on the Euler-Lagrange formulation, the source terms for the Eulerian equations are obtained, which then can be solved to compute the reactive gas-phase behaviour during ignition and combustion. This facilitates the prediction of the reactive behaviour of the solid fuel particles in more complex configurations using direct numerical simulations, which can provide data inaccessible in the experiments. In this section, the application of the point-particle approximation to capture the underlying physics behind the ignition and combustion of single particles and particle groups in laminar conditions is presented.

Modelling Single Particle Combustion

The first step in predicting the correct behaviour of solid fuel particles in a reactive environment is predicting the ignition time. Particle geometry, internal structure, elemental composition, and operating conditions of the burner can significantly impact the ignition and combustion processes. Therefore, it is essential first to investigate the effect of these parameters on the ignition and combustion of single particles in a laminar flow reactor configuration, in which multi-parameter optical measurements provide experimental data for validation of the numerical framework. This configuration is described in detail in Chap. 10. Solid fuel type (coal or biomass) is one of the most important parameters affecting ignition. Due to the different characteristics of biomass compared to coal, the combustion behaviour of biomass particles is expected to be different than that of coal. Therefore, in this section, the reactive behaviour of different solid fuel types is compared. In this context, single high-volatile bituminous Colombian coal (CBC) and walnut shell biomass (WNS) particles have been chosen for this comparison. The respective solid fuel composition for these fuels can be found in Table 1.1.

Since modelling ignition and combustion of solid particles requires a significant number of physical models and simplifying assumptions, a validation of ignition delay times of single particles with available experimental measurements [6] is presented. The comparison with the experiments displayed in Fig. 12.2 shows good agreement with measured ignition delay times for variations in particle diameter D_p. In the simulations, ignition delay time τ_{ign} is defined as the point when the mass fraction of OH radicals Y_{OH} exceeds 5% of its maximum. This definition is consis-

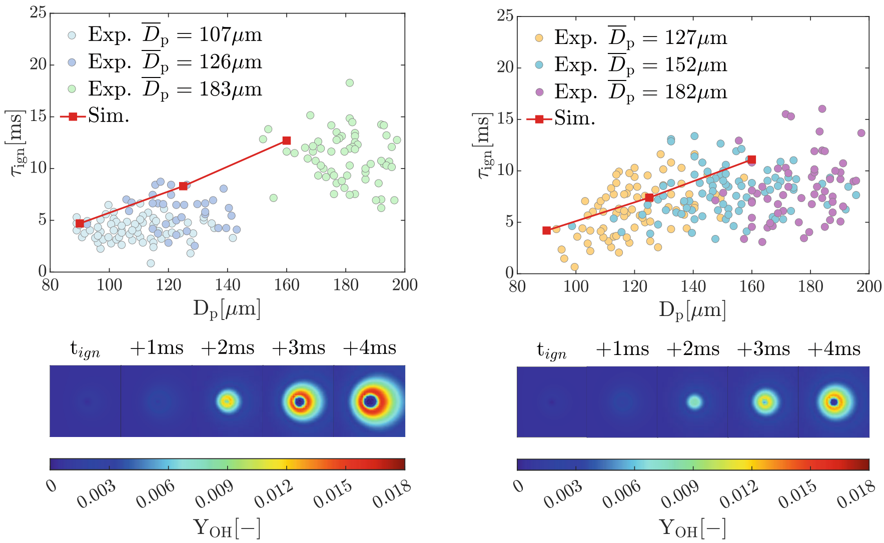

a) CBC **b)** WNS

Fig. 12.2 Ignition delay times τ_{ign} for various particle sizes compared with experimental data reported by Li et al. [6] (top row) and evolution of Y_{OH} after ignition for a single particle with $D_p = 125\,\mu m$ (bottom row) for **a)** CBC particles and **b)** walnut shell particles

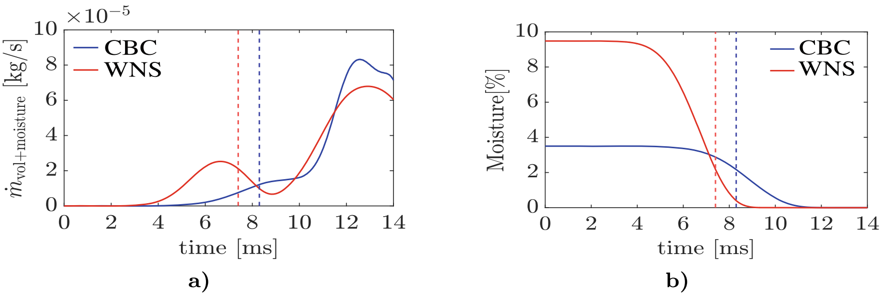

Fig. 12.3 **a)** Evolutions of total devolatilisation and evaporation rate ($\dot{m}_{\mathrm{vol+moisture}}$), and **b)** remaining moisture content of CBC in comparison with walnut shell during ignition and combustion of single particles with $D_{\mathrm{p}} = 125\,\mu\mathrm{m}$. Vertical dashed lines show the ignition times respectively

tent with the experimental definition of the ignition event based on the imaged flame intensities (by OH-LIF) exceeding the background level.

The comparison between the coal and walnut shell ignition shows a slightly faster ignition for walnut shells compared to coal particles. Additionally, as shown in Fig. 12.2, walnut shell particles have a weaker flame with lower OH intensity around the particle compared to coal. This is related to the lower amount of released mass during devolatilisation for walnut shells compared to coal due to the lower apparent density in walnut shells [6].

The lower apparent density of the walnut shells compared to coal alongside with the higher volatile content based on the proximate analysis of these fuels reported by Li et al. [6] is expected to significantly increase the particle heating rate and reduce the ignition delay time. Although, as shown in Fig. 12.3, the higher amount of moisture for biomass particles, which must be evaporated before the release of fuel species, and is known to delay the ignition process are the primary reasons for the similarity in ignition behaviour between coal and walnut shells because of a cancellation of competing effects between drying and volatile release processes.

After studying the ignition characteristics, the flame structure is further investigated by analysing the flame stand-off distance from the particle surface as shown in Fig. 12.4a). In this context, the stand-off distance r_{f} is defined as the distance from the particle surface at which peak activity $Y_{\mathrm{OH,max}}$ occurs. This distance is normalised by the particle radius r_{p} to yield a dimensionless measure. When considering volatile combustion in a diffusion regime, the chemical reaction is relatively faster than mass and thermal diffusion. The flame location is then determined by two key factors: the volatile release and the oxygen diffusion [6]. Increasing the particle size leads to lower particle heating rate and consequently lower devolatilisation per unit area, as shown in Fig. 12.4b), which results in the flame burning closer to the particle surface. In the comparison of the flame distance between coal and biomass, the main reason is the higher released mass per unit area from the coal particles compared to walnut shells.

In order to investigate the effect of oxygen diffusion on the flame location with respect to particle surface, the flame stand-off distance at different oxygen content of 10, 20, and 40% in air atmosphere are compared for walnut shells with the same particle size. Figure 12.5a) depicts a smaller stand-off distance for the flame for

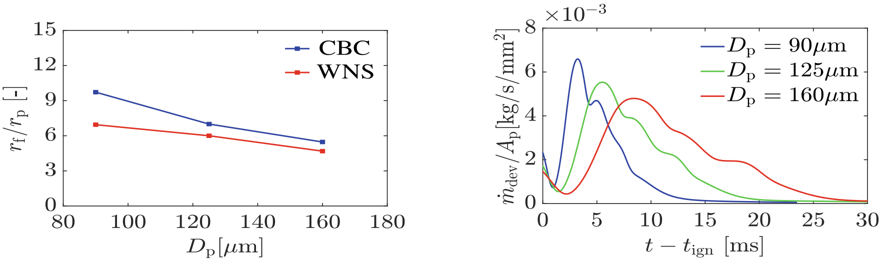

a) **b)**

Fig. 12.4 **a)** Effect of particle size D_p in normalised flame distance r_f/r_p of coal and walnut shells in air and **b)** volatile release rate per particle surface area for walnut shell particles with increasing particle diameter

higher oxygen contents for both coal and biomass. Higher oxygen contents increase the O_2 diffusion towards the particle surface. Also, this will increase the reactivity of the mixture by producing more radicals based on $O_2 + H \rightarrow OH + O$, which is the most important chain branching reaction for combustion. This leads to increasing the gas-phase temperature in the vicinity of the particle and, as a result, a higher devolatilisation rate per unit area as shown in Fig. 12.5b). Therefore, it can be concluded that the O_2 diffusion rate effect is stronger than the volatile release rate and can significantly impact the flame structure.

More detailed information regarding the differences between the ignition and combustion characteristics of single coal and biomass particles can be found in the study by Li et al. [6].

Modelling Particle Group Combustion

In addition to the study of single particles, the ignition process of particle streams in air and oxy-fuel atmospheres needs to be studied. To investigate the effect of interacting volatile flames, the laminar hot co-flow particle stream configuration based on the laminar flat flame burner experiment [7], is presented. This configuration is a 3-D channel with inlet and outlet boundaries in the stream-wise direction, while

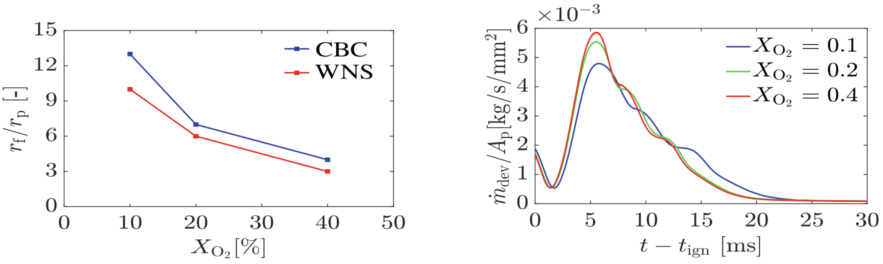

a) **b)**

Fig. 12.5 Effect of oxygen content on **a)** r_f of coal and walnut shells in air and **b)** volatile release rate per particle surface area for walnut shell particles

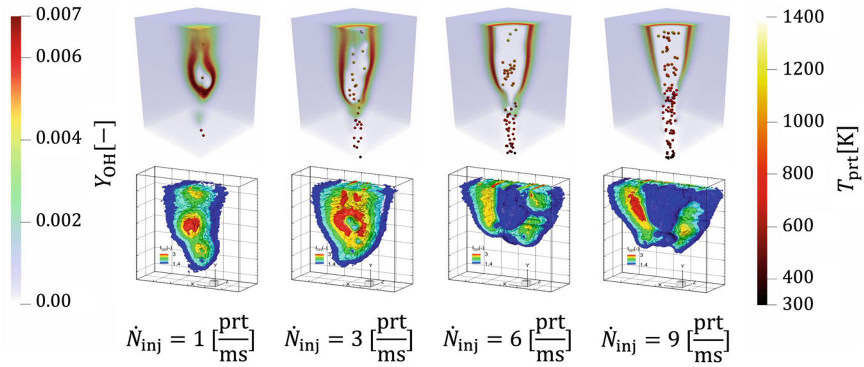

Fig. 12.6 Flame shapes visualised by OH mass fraction and particle temperature at statistically steady-state conditions in the co-flow jet configuration at different particle injection rates (top row) compared with experimental 3-D OH-LIF signals for the corresponding particle injection rates [8] (bottom row) (reprinted from Farmand et al. [9], Copyright (2022), with permission from Elsevier and minor editing)

periodicity is imposed in the two span-wise directions. Solid fuel particles are seeded directly into a hot oxidiser stream for the channel configuration inlet. This configuration is representative of a typical industrial burner, where the mixing time is faster than the particle heating time.

After injection, due to the heat transfer between particles and the gas phase, particles heat up, and their temperatures gradually increase. Moving further downstream, at a certain distance from the inlet for each case, volatile ignition occurs, which can be identified with the increase in OH radical in the domain. The ignition delay time can be determined after reaching a statistically steady state by means of the ignition position and the averaged particle velocity for different cases of varying particle number density, gas temperature, and injection velocity. Figure 12.6 shows the OH radical fields visualising the flame for different particle injection rates in comparison with the experimental 3-D OH-LIF measurements by Li et al. [8]. Analysing the numerical and experimental OH radical fields demonstrated a transition in ignition location and flame topology from single particles towards dense particle streams. It was observed that increasing the particle injection rate, which leads to higher local particle number density in the domain, shifts the ignition location downstream and increases the ignition delay time because of the increased amount of thermal energy needed for particle heating. The in-depth analysis of the physical processes occurring during this transition highlights that increasing the particle injection rates affects the volatile flame shape, devolatilisation rate, velocity profile, and particle distribution. At low particle injection rates, the volatiles mainly burn in diffusion flames formed around individual particles similar to the single-particle behaviour studied by Farazi et al. [5]. By increasing the particle injection rate, due to oxygen deficiency and relatively lower gas temperatures around the centreline, a delay in the ignition and a more continuous flame region around the particle clouds were observed. This behaviour is more pronounced for higher particle injection rates, in which the flame is suppressed

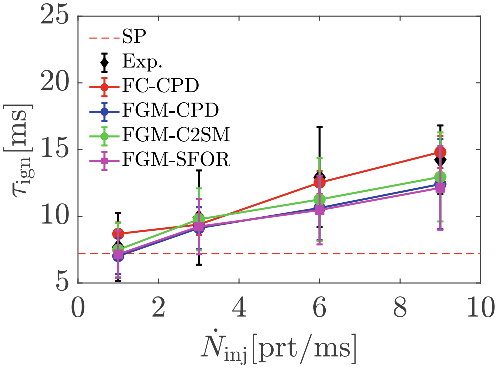

Fig. 12.7 Comparison of computed ignition delay times in detailed simulations (FC-CPD) with experiments and FGM model predictions with different devolatilisation models (FGM-CPD, FGM-C2SM, FGM-SFOR) for different injection rates. The error bars corresponds to different thresholds of Y_{OH}. The horizontal dashed red line correspond to detailed single particle (SP) simulation reprinted from Farmand et al. [9], Copyright (2022), with permission from Elsevier and minor editing)

in the centre and consequently limited to the area in the boundary region, where the ignitable mixtures are formed due to the mixing of volatiles with the oxidiser [2,9].

In addition to the investigation of physical processes, the complete thermochemical state can be extracted from detailed simulations, which allows for the detailed assessment of the reduced-order models for particle group ignition and combustion. Therefore, different modelling assumptions for devolatilisation, ignition, and combustion were also assessed. To this end, the performance of reduced order gas-phase chemistry utilising flamelet generated manifolds (FGM) model and reduced-order particle devolatilisation using CPD, C2SM, and SFOR models in comparison with detailed simulations (finite rate chemistry and CPD (FC-CPD)) was evaluated. As shown in Fig. 12.7, the detailed model simulations (FC-CPD) for both gas and solid phases were successfully validated with the experimentally measured ignition times by Li et al. [8].

It was also observed that the predicted ignition by the simulations using different simplified modelling assumptions for gas-phase and particle devolatilisation (FGM-CPD, FGM, C2SM, FGM-SFOR) agrees well with the experimental data. However, due to the simplified assumptions and model inaccuracies, these reduced-order models under-predict ignition times compared to the detailed model (FC-CPD). To investigate the most reduced-order model (FGM-SFOR) inaccuracies compared with the most detailed model (FC-CPD) and to evaluate the assumptions involved in pulverised fuel FGM modelling, a comprehensive investigation of each reduction step using a systematic model simplification approach was employed. In the detailed simulations, the dynamic volatile composition CPD model is used [5]. In contrast, the typically applied FGM formulation is limited to using a fixed volatile composition to create the flamelet tables. It was found that using this simplifying fixed volatile composition assumption leads to a shift in the release of different volatiles. However, it has a minor effect on particle group ignition, which shows the validity of this assumption for this case [9]. In contrast, the comparison of radial gas-phase

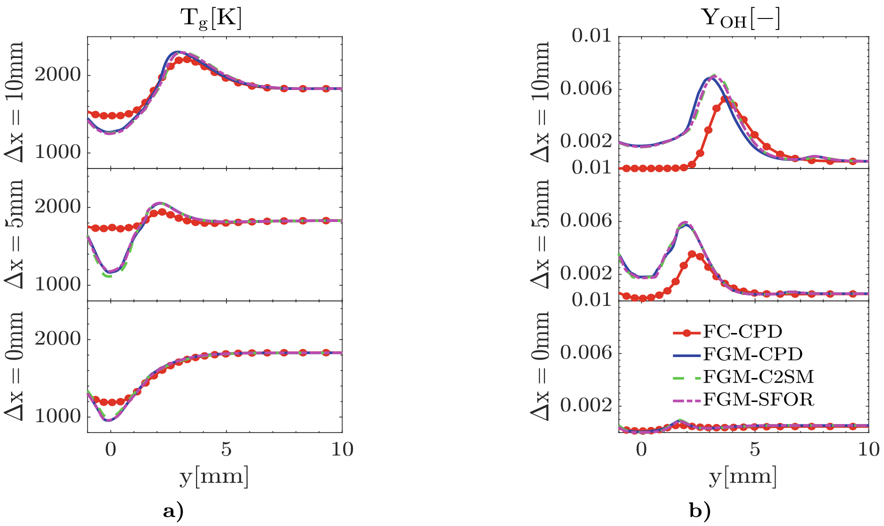

Fig. 12.8 Effect of different reduced order solid- and gas-phase models (FGM-CPD, FGM-C2SM, FGM-SFOR) in prediction of radial mean profiles of **a)** gas-phase temperature and **b)** OH mass fraction at different axial distances from the ignition height (Δx) for particle group configuration with $\dot{N}_{\mathrm{inj}} = 6\mathrm{ms}^{-1}$ compared to detailed simulations (FC-CPD) (reprinted from Farmand et al. [9], Copyright (2022), with permission from Elsevier and minor editing).

temperature and OH mass fraction profiles at different heights above the ignition location, as shown in Fig. 12.8 demonstrated that tabulated chemistry has deficits, especially in the central region, where the fuel-rich mixture exceeds the flammability limits and extrapolation in the flamelet table is used.

It should be noted that simplified yet well-fitted devolatilisation models (C2SM and SFOR) can perform similarly compared to detailed devolatilisation model (CPD). However, as the parameters are quite sensitive to the heating rate, the quantitative agreement is very dependent on the heating rates used for fitting the parameters. Detailed analyses are presented in the study by Farmand et al. [9].

12.4 Modelling Ignition and Combustion of Solid Fuels Under Turbulent Conditions

Different studies of single-particle and particle group ignition in laminar conditions show that the slip velocity significantly impacts ignition [2, 10, 11]. When particles are exposed to turbulent conditions, they face different slip velocities due to the velocity fluctuations in a turbulent flow, which significantly impact the particle ignition behaviour. In the following sections, first, the physical aspects of the particle cloud ignition under turbulent conditions are investigated. Then, the available models and their applicability for predicting the ignition process in the particle clouds are discussed. It should be mentioned that the general conclusion of this chapter is valid for both high-volatile coal and biomass fuels since both fuels exhibit similar combustion characteristics, as shown in Sect. 12.3.

To understand the effects of turbulent velocity fluctuations on particle ignition and combustion, the homogeneous isotropic turbulent (HIT) configuration is employed to remove the complexities caused by turbulent shear forces.

Due to the absence of mean gradients, HIT has no turbulence production, and as a result, turbulence decays in time. Therefore, the effect of turbulence interactions on the ignition and the combustion process was investigated utilising a fully developed HIT field with a linear forcing in physical space [12] to keep turbulence in a statistically steady state during ignition and combustion [13]. The motion of particles in turbulent flows depends on the time scales of turbulence and particle inertia. Since solid fuel particles have a much higher density than the surrounding gas, they do not fully follow the flow. This behaviour leads to preferential particles concentrations in turbulent flows. This phenomenon typically occurs when the characteristic particle time is in the same order as the flow time scale and is defined by the Stokes number. When the Stokes number is around unity, particles tend to form clusters, resulting in regions almost void of particles [14]. Such preferential concentration can occur in practical applications and has a significant effect on particle ignition process, which is investigated in this section.

12.4.1 Particle/Turbulence Interaction Effects on Ignition

In this analysis, turbulence characteristics and particle size were chosen so that particle preferential concentration could be observed. In addition, these conditions can represent the smaller-scale turbulent fluctuations under practically relevant conditions [15,16]. To study the preferential concentration of the particles, 10,000 CBC particles (see Table 1.1) with $D_\mathrm{p} = 20\,\mu\mathrm{m}$ and $T_{\mathrm{p},0} = 300\,\mathrm{K}$ and with an apparent density of $700\,\mathrm{kg\,m^{-3}}$ are randomly initialised in the forced HIT environment with $\eta \simeq 100\,\mu\mathrm{m}$ and the physical size of $12.8 \times 12.8 \times 12.8\,\mathrm{mm}^3$ with periodic boundary conditions in all directions. Air with 20% oxygen and an initial gas temperature of $T_{\mathrm{g},0} = 1500\,\mathrm{K}$ was chosen as an oxidiser, which is relevant to solid fuel combustion practical applications. To quantify the ignition process, an ignition onset needs to be defined. Typically, a certain OH radical threshold is utilised to identify the ignition onset in joint numerical-experimental studies based on OH-LIF measurements [7,9].

In the current complex turbulent configuration, due to non-existing experimental measurements, a definition for the ignition similar as in the previous section was used [9]. The flame characteristics are not significantly affected by the choice of OH mass fraction thresholds used to define ignition. This definition was also employed in previously validated studies [9,17] to quantify the ignition onset in comparison with experimentally measured ignition delay time, was used to ensure having a realistic benchmark for the analysis.

The clustering of the particles leads to increased local particle number density at specific locations and, as a result, reduced gas temperature at those locations due to the

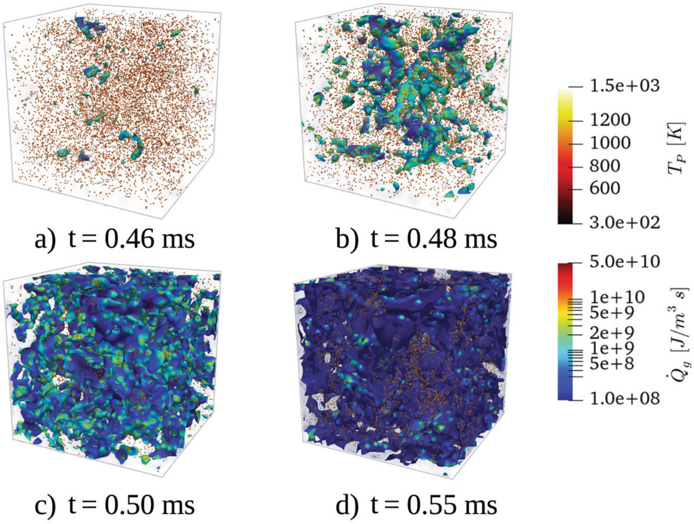

Fig. 12.9 Evolution of the ignited regions illustrated by the iso-surfaces of the 10% of the maximum Y_{OH} during the entire combustion process coloured by heat release rate. Particles are marked with spherical points coloured by particle temperature (reprinted and slightly adapted from Farmand et al. [13], licensed under CC BY 4.0)

energy sink required for heating up the particles. Also, higher oxygen availability in these regions results in more favourable thermo-chemical conditions for ignition. The ignited regions can then spread similarly to the laminar flame described in Sect. 12.3 through the entire domain by the growth and merging of individual ignited kernels. The evolution of the ignited region in HIT configuration is depicted in Fig. 12.9.

The particle preferential concentration can be quantified using the Voronoi algorithm [13, 18]. In the Voronoi algorithm, the domain volume is discretised by the Voronoi cells, which are created based on the distance between each two adjacent particles [18]. After discretising the domain by the Voronoi cells, the clustering volume threshold V_{C} can be obtained by comparing the normalised Voronoi volume distribution in the clustered field $P(V/\overline{V})$ with a randomly distributed particle field $P(V_{\mathrm{R}}/\overline{V})$, in which $\overline{V}$ in the average Voronoi cell volume, calculated based on the Voronoi volume around each particle [18]. Analysing the first ignited regions in the Voronoi space as illustrated in Fig. 12.10a) quantitatively shows that the first ignition kernels predominantly occur outside of particle clusters, where a higher number of ignited points can be observed at volumes larger than clustering limit V_{C}. It was found that the higher gas temperatures outside of particle clusters are the main reason for this ignition behaviour [13]. A detailed description of calculating the clustering limit can be found in the study by Farmand et al. [13].

Calculating the number and the volume of ignited regions during ignition as shown in Fig. 12.10b) can quantify the evolution of the ignition process from auto-ignition to interaction ignition [13]. At interaction ignition, no new individual ignition kernels

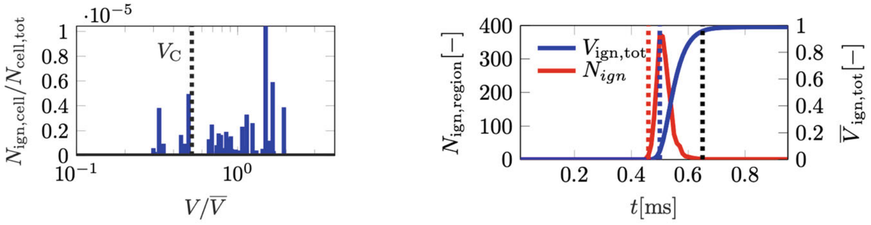

a) **b)**

Fig. 12.10 **a)** Normalised number of the ignited cells in normalised Voronoi volumes at $\tau_{\mathrm{auto.ign}} \simeq 0.46$ms. Vertical dashed line shows the clustering threshold V_{C}. **b)** Evolution of the number of separated ignited regions (N_{ign}) and the total normalised volume $\sum V_{\mathrm{ign}}$ of the ignited regions. The vertical red, blue, and black dotted lines show the auto-ignition time, interaction ignition time, and end of the ignition process (reprinted and slightly adapted from Farmand et al. [13], licensed under CC BY 4.0)

are formed, and flame propagation occurs due to the rapid merging and growth of the ignited regions, resulting from heat release rate from the ignited regions [19].

12.4.2 A Priori Model Assessment and Flamelet Modelling of Ignition

The particle cloud ignition process is inherently transient, and the presence of particle preferential concentration further affects the reactivity [20]. Therefore, it is essential to carefully evaluate the assumptions made in reduced-order models to correctly predict ignition and flame characteristics during solid fuel combustion. In this section, a systematic model assessment based on error decomposition method described in the work from Farmand et al. [13] is used to evaluate the model's overall performance from different perspectives. To this end, the flamelet/progress variable (FPV) model is assessed compared to DNS to quantify the suitability of the tabulated thermochemical state. The main focus of this study was placed on modelling the progress variable source term ($\dot{\omega}_{\mathrm{C}}$) as the quantity of interest to predict particle cloud ignition and combustion. The reference progress variable is defined by Farmand et al. [13] and Nicolai et al. [15] as

$$\mathcal{C}_{\mathrm{ref}} = Y_{\mathrm{CO_2}}/\mathcal{M}_{\mathrm{CO_2}} + Y_{\mathrm{CO}}/\mathcal{M}_{\mathrm{CO}} - Y_{\mathrm{O_2}}/\mathcal{M}_{\mathrm{O_2}}, \tag{12.13}$$

where $\mathcal{M}_i$ is the molar mass of species i.

The progress variable source term in the FPV model shows a shift compared to the DNS, which indicates over-prediction of ignition delay time by the FPV model [13]. To understand the origin of this ignition deviation in the FPV model from the DNS results, the model's performance inside and outside the particle clusters during ignition needs to be studied in more detail. To this end, $t = 0.5$ ms with the maximum number of ignited regions during the ignition process, is shown in Fig. 12.10b).

The optimal estimator concept is used to quantify the errors inside and outside of particle clusters [13]. The reduced-order modelling of unclosed terms in partial differential equations typically involves two steps: First, a set of input parameters should be specified for the model, and second, a specific functional form needs to be defined to model the unclosed terms by the input parameters [21]. Each of these steps introduces errors that need to be carefully investigated in the model assessment process. The error corresponding to the first step is known as the irreducible error, while the error corresponding to the second step is referred to as the functional error. The total modelling errors, computed by the overall difference between the quantities of interest obtained by the model and the DNS, can be systematically decomposed using the optimal estimator method into irreducible and functional errors. The general idea of the optimal estimator concept is to determine for a given parameter set Π, the mean of a quantity of interest ϕ conditioned on the set of parameters $\langle \phi \mid \Pi \rangle$ and obtain a measure for the scatter of the quantity of interest with respect to Π. Formally, the irreducible error is given by Berger et al. [21] as

$$\epsilon_{\mathrm{irr}}^2 = \left\langle (Q_{\mathrm{int}} - \langle Q_{\mathrm{int}} \mid \Pi \rangle)^2 \right\rangle . \qquad (12.14)$$

In the following, irreducible error ϵ_{irr} and the error caused by the functional form of the model ϵ_{func}, are discussed for identifying the potential for model improvements. First, the model parameters chosen to parameterise the flamelet table are assessed using the optimal estimator method. This enables the calculation of irreducible errors for different sets of input parameters to predict the quantity of interest.

Figure 12.11a) demonstrates that the inclusion of the progress variable and enthalpy alongside the mixture fraction strongly decreases the overall irreducible error, especially inside the clusters, where the errors are the highest. Finally, it can be concluded that the combination of mixture fraction Z, progress variable C_{n}, and enthalpy h_{n} leads to the smallest irreducible error. Using these parameters as the best set of input parameters, a non-premixed flamelet table can be generated as described in Farmand et al. [13]. The progress variable source term predicted from the FPV model can be compared with the corresponding value from the DNS datasets to cal-

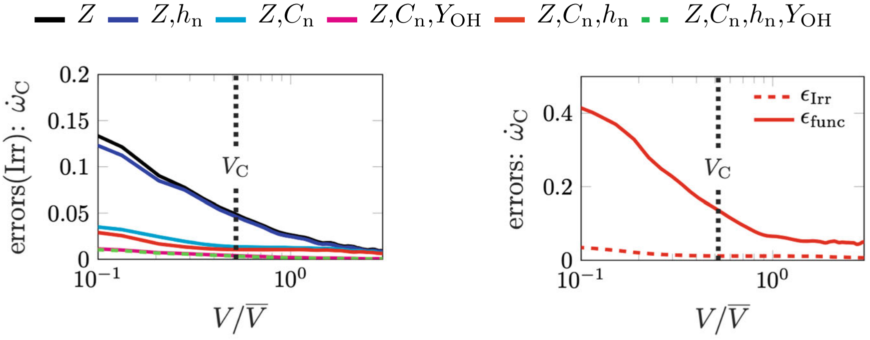

a)

b)

Fig. 12.11 **a)** Irreducible errors of different input parameters and **b)** decomposed errors involved in the reference FPV model in comparison with the DNS results in the prediction of progress variable source term (reprinted and slightly adapted from Farmand et al. [13], licensed under CC BY 4.0).

Table 12.1 Different flamelet tables input combinations

Input parameter combinations	Definition of $\mathcal{C}$
Z, C_n, h_n	$\mathcal{C}_{\mathrm{ref}}$
Z, C_n	$\mathcal{C}_{\mathrm{ref}}$
$Z, C_{n,1}, h_n$	$Y_{\mathrm{CO_2}} + Y_{\mathrm{CO}}$
$Z, C_{n,2}, h_n$	$Y_{\mathrm{CO_2}} - Y_{\mathrm{O_2}}$
$Z, C_{n,3}, h_n$	$Y_{\mathrm{CO_2}}/\mathcal{M}_{\mathrm{CO_2}} + Y_{\mathrm{H_2O}}/\mathcal{M}_{\mathrm{H_2O}} - Y_{\mathrm{O_2}}/\mathcal{M}_{\mathrm{O_2}}$

culate the functional errors as shown in Fig. 12.11b). The analysis shows that the particle clusters significantly affect the functional modelling errors. The overprediction of the progress variable source term inside the particle clusters can be attributed to the limitations of the typically used flamelet tabulated chemistry models in capturing the particle/chemistry interactions. This limitation is especially prominent in the vicinity of particle clusters, which corresponds to a smaller mixing time scale compared to the chemical time scale. In these regions, where the volatiles mix with the oxidiser prior to ignition, the flame behaviour resembles that of a premixed flame, which the non-premixed flamelet approach cannot accurately capture [13].

In the next step, the effects of changing the input parameters, such as excluding enthalpy and altering the progress variable definition in the model performance, are also examined. In order to investigate the effect of heat losses and the progress variable definition in the model, different flamelet tables with various input parameter combinations are generated. The input parameters of these different flamelet tables are summarised in Table 12.1.

From Fig. 12.12a), it is evident that including enthalpy in the flamelet table primarily affects the predictions. In particular, incorporating enthalpy as an input parameter improves the accuracy of the model inside the clusters, especially during ignition. This suggests that the ignition phase is sensitive to changes in enthalpy, especially

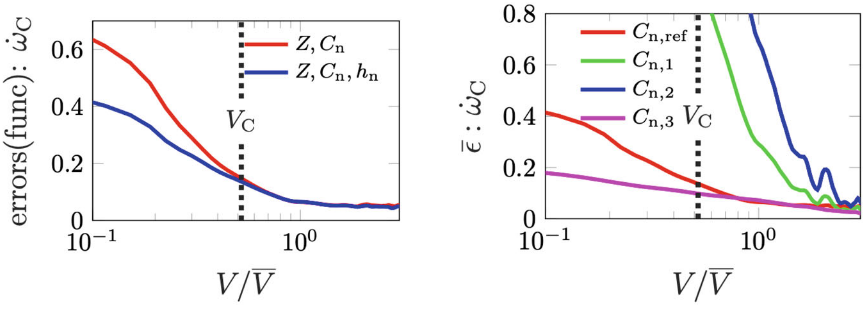

a) b)

Fig. 12.12 **a)** Effect of enthalpy and **b)** effect of progress variable definition in the errors of progress variable source term. Solid colour lines show the functional errors, and dashed colour lines correspond to irreducible errors. Volumes larger than V_C represent regions outside of clusters (reprinted and slightly adapted from Farmand et al. [13], licensed under CC BY 4.0).

inside the clusters. During the ignition phase, due to the particle heat-up process and the higher temperature gradients between particles and the gas phase, the heat loss effect is more dominant than at later times [17].

Altering the definition of progress variables can also affect the model's performance. As shown in Fig. 12.12b), excluding CO or O2 from the model significantly amplifies the functional errors of predicting the progress variable source term ($\dot{\omega}_\mathrm{C}$), indicating that $C_{\mathrm{n},1}$ and $C_{\mathrm{n},2}$ are not suitable choices for representing the progress variable. On the other hand, replacing CO with H_2O ($C_{\mathrm{n},3}$) resulted in an improvement in predicting the progress variable source term, particularly within the clusters. This shows that the definitions of the input parameters are as important as the combination of the input parameters in the flamelet table in the correct prediction of quantities of interest. More detailed analysis regarding the a priori model assessment of ignition in clustering particle clouds can be found in the study by Farmand et al. [13].

12.5 Modelling Pollutant Formation During Solid Fuel Combustion

In solid fuel combustion, controlling hazardous NO_x is one of the major challenges. Unlike gas hydrocarbon combustion, solid fuels contain fuel-bound nitrogen, which is the primary source of NO_x. When particles are exposed to heat, the internal bounds inside the particle structure break and the nitrogen element is released as small nitrogen-containing species, which are considered to be the main NO_x precursors. This is a complex and multi-physics process and experiments are limited to providing detailed information regarding the pathways involved. Therefore, numerical simulations with the detailed kinetic models for both solid and gas phases, including the reaction pathways for NO_x can provide additional valuable insights. In this study, solid kinetics is modelled using the CRECK-S model as described in Sect. 8.2.3 and the gas-phase chemistry is modelled with the recently developed Complete-ITV-NO_x chemical kinetic model [22]. A detailed description of these kinetic models can be found in Sects. 8.2.3 and 6.3. This section analyses NO_x formation for single particle and particle group combustion in laminar conditions.

12.5.1 NO_x Formation During Ignition and Combustion of Solid Fuels

Since NO_x formation in solid fuels involves kinetic models for both solid and the gas phase, the performance of these models first needs to be assessed compared to available experimental measurements. The drop tube furnace (DTF) configuration, described in Sect. 2.2.3, is typically utilised for measuring NO_x during solid fuel combustion. In the chosen drop-tube furnace, particles with the size of $D_\mathrm{p} = 90\,\mu\mathrm{m}$ are released from the injector with a specific mass flow rate at the top of a long furnace with high gas-phase temperature. Due to the long residence time, the complete

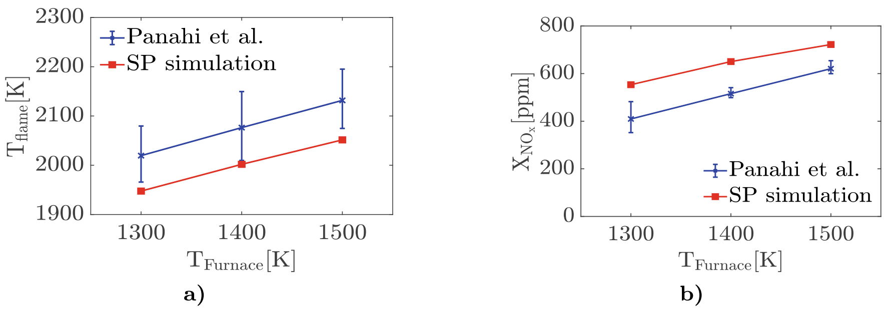

Fig. 12.13 Comparison of the **a)** flame temperature and **b)** time- and space-averaged model predictions for mole fraction of NO_x for single Pittsburgh coal (USC) particles at different furnace temperatures compared to the experimental data by Panahi et al. [24]

process of ignition, combustion, and NO_x formation can be observed and the species concentrations can be measured at the end of the tube [23].

However, performing direct numerical simulations of a full DTF geometry is numerically expensive. Therefore, these simulations are typically performed in a downscaled inherited DTF geometry, for which the dimensions are chosen such that the domain size is large enough to contain the full flame characteristics from ignition to complete combustion [22]. In this study, NO_x formation during single particle and particle groups combustion is investigated. The furnace operating conditions, particle sizes, and mass flow rate for the particle group configuration is chosen to match that of the experiments [23, 24]. Also, to assess the NO_x emissions, simulations were conducted for two flow-through times, which leads to a statistically steady-state for NO_x concentration at the exit plane.

Due to the utilised adopted geometry of the experimental configurations and due to the uncertainties in the numerical models and experimental boundary conditions, only the trends were compared with the measurements. For evaluating the performance of the numerical framework, flame temperature and the time- and space-averaged NO_x at the exit plane for high volatile bituminous Pittsburgh coal (USC) (see Table 1.1) was calculated for comparison with the experiments performed by Panahi et al. [24]. It is worth noting that the simulation results for NO_x mole fractions are scaled by the ratio of the experimental cross-sectional area to that of the simulation so that the volumetric flow rates are the same in both the simulations and experiments. As shown in Fig. 12.13, the trend of the experimental data for flame temperature and NO_x mole fractions can be reproduced, which shows the validity of the numerical framework in capturing the sensitivity of NO_x with respect to different operating parameters. Figure 12.13a) also shows that increasing temperature leads to an increase of NO_x formation, which is due to the increased reactivity in the NO_x formation pathways [22].

After evaluating the numerical framework performance in capturing the NO_x sensitivity with respect to different operating parameters, the comprehensive datasets generated from DNS can be used to study the NO_x production and consumption pathways. To gain a deeper understanding of the NO_x formation process, the reaction pathways are quantitatively analysed using the reaction flux analysis in the next section.

12.5.2 NO_x Formation Pathway Analysis

The NO_x formation is inherently a transient process. To obtain a global view of this transient production and consumption pathways, reaction path analysis (RPA) and rate of production analysis (ROPA) for the nitrogen element flux should be performed. The nitrogen element flux $\dot{N}_{AjB}$ from species A to B through reaction j is defined by Farmand et al. [22] and Shamooni et al. [25] as

$$\dot{N}_{AjB} = \frac{n_{N,A}\, n_{N,B}}{n_{N_R,j}}\, \dot{r}_j, \tag{12.15}$$

where $n_{N,A}$ and $n_{N,B}$ are the numbers of nitrogen atoms in species A and B considering the corresponding stoichiometric coefficients. The term $n_{N_R,j}$ represents the sum nitrogen atoms on either side of reaction j, while $\dot{r}_j$ is the net rate of reaction in a chemical mechanism with N_s species and N_r reactions, defined as

$$\dot{r}_j \equiv k_{f,j} \prod_{k=1}^{N_s} \left(\frac{\rho Y_k}{W_k}\right)^{\nu'_{k,j}} - k_{b,j} \prod_{k=1}^{N_s} \left(\frac{\rho Y_k}{W_k}\right)^{\nu''_{k,j}}, \tag{12.16}$$

where $\nu'_{k,j}$ and $\nu''_{k,j}$ are the molar stoichiometric coefficients of species k in forward and backward reactions, with Arrhenius rates of $k_{f,j}$ and $k_{b,j}$, respectively.

Following [26], who introduced the time-integrated element flux analysis, all of the analyses in this study are performed using time- and volume-integrated (averaged) fluxes over the entire numerical domain and the total simulation time.

12.5.3 NO_x Formation Pathways for Coal and Biomass

As mentioned in Sect. 12.3, the solid fuel type can significantly impact the overall reactive behaviour of solid pulverised fuels. The solid fuel type can change the volatile mixture composition, which can affect the reactions in the gas phase and consequently impact the NO_x formation pathways. To study the effect of fuel type, NO_x formation pathways during the combustion of the high volatile Pittsburgh coal (USC) particles and torrefied miscanthus (TMG) biomass particles are compared. A detailed characterisation of these fuels can be found in Table 1.1. Single particle simulations for the selected coal and biomass types at $T_\mathrm{g} = 1400$ K with a similar particle size of $D_\mathrm{p} = 90\,\mu\mathrm{m}$ in a drop tube configuration described in Sect. 12.5.1 were performed to study the effect of solid fuel type on NO_x formation pathways. Based on the ultimate analysis comparison of Pittsburgh coal and torrefied miscanthus, higher nitrogen content in the coal particle will lead to a higher NO_x formation compared to miscanthus [22]. In this section, the NO_x formation pathways are discussed in more

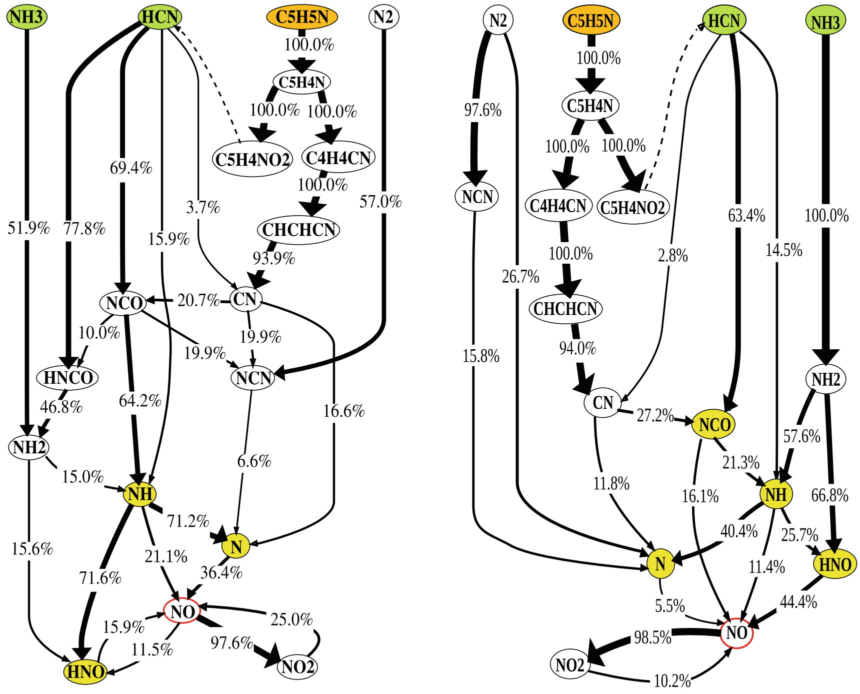

a) USC
b) TMG

Fig. 12.14 The most important time- and space-averaged pathways of N atoms from the released nitrogen-containing volatiles (NH_3, HCN, and C_5H_5N) and N_2, which contribute to NO production for **a)** USC and **b)** TMG biomass. The N-containing light gases (NH_3 and HCN) are coloured green and N-containing tar (C_5H_5N) is coloured orange. Direct N-containing radicals (N, NH, HNO) are coloured yellow

details. RPA for the nitrogen element flux from the nitrogen-containing volatiles and N_2 towards NO_x as illustrated in Fig. 12.14 shows the most important pathways for NO_x formation. The percentage beside each arrow corresponds to the locally normalised flux of N atoms between two species by the total incoming fluxes. The thickness of each arrow is proportional to the N-flux in each path. Some minor pathways are neglected and removed to increase clarity. This approach for presenting the RPA is similar to the method described by Shamooni et al. [25]. It is worth noting that in direct NO production, similar N-containing radicals (NH, N, HNO) participate in both Pittsburgh coal and miscanthus. However, in miscanthus combustion, NCO, which originates from the direct decomposition of HCN, also participates in the direct production of NO. In addition, unlike coal, in which N is the most dominant radical for direct NO production, HNO is the dominant radical in miscanthus combustion. However, both N and HNO originate from the NH radical and it can be concluded that NH is the most important radical for NO production during coal and miscanthus combustion. The most important reactions in NO production and consumption can be studied using the rate of production analysis. Based on the rate of production

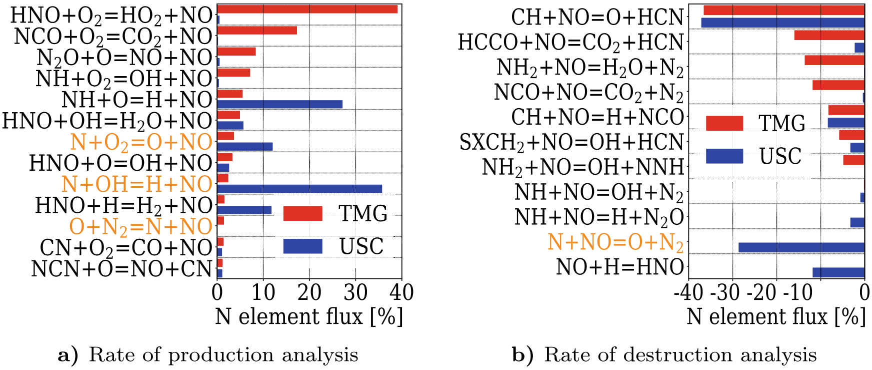

a) Rate of production analysis **b)** Rate of destruction analysis

Fig. 12.15 Rate of NO **a)** production and **b)** destruction analysis for coal and miscanthus. The extended Zeldovich reactions are coloured orange

of NO, as shown in Fig. 12.15a), although similar N-containing radicals participate in direct NO production, the NO formation pathways are completely different in coal compared to biomass. It can be observed that $HNO + O_2 \rightleftharpoons HO_2 + NO$ is the most important reaction for miscanthus. In contrast, during coal combustion, $N + OH \rightleftharpoons NO + H$ is the dominant reaction. This difference originates from different volatile compositions released from the Pittsburgh coal and miscanthus.

The rate of destruction analysis of NO, as shown in Fig. 12.15b), also highlights that NO destruction during miscanthus combustion, occurs primarily in contact with small hydrocarbon radicals such as H, CH, HCCO through the so-called reburn mechanism [22]. However, during coal combustion, the N radical is the most important radical for NO destruction through reaction $N + NO \rightleftharpoons O + N_2$. This reaction is the initiation reaction for the Zeldovich mechanism for thermal-NO_x pathways. The net NO production rate shows that this reaction only contributes to less than 10% of the total NO formation. Therefore, it can be concluded that the thermal-NO_x pathways have a minor impact on the overall NO formation during single-particle coal and miscanthus combustion.

12.5.4 Effect of Particle/Particle Interactions on NO_x Formation

After investigating the NO_x formation pathways in single-particle configuration, the particle/particle interaction is studied by comparing the reaction pathways in the particle group configuration and the single particle configuration. Besides varying the total nitrogen mass in the furnace, particle number density can impact the reaction pathways by changing the particle/particle/chemistry interactions. To this end, simulations of a miscanthus particle group with the same boundary conditions and particle size as the single particle configuration were performed to suppress the impact of other operating parameters in the analysis. It should be mentioned that due to the transient nature of the NO_x formation, the particle group simulation was also performed with a long enough residence time ($t = 330$ ms) so that NO_x mole fraction

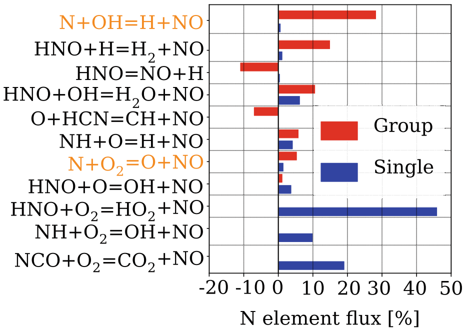

Fig. 12.16 Effect of particle/particle interactions on the production rate of NO averaged over the entire computational domain and simulation time. The extended Zeldovich reactions are coloured orange

reaches a statistically steady state at the burner exit plane. Rate of production analysis as shown in Fig. 12.16 highlights the fact that the particle group configuration has a completely different reaction pathway for NO formation, which underscores the importance of particle/particle interactions in NO emissions.

In particle group configuration, unlike the single-particle configuration, the reaction $\mathrm{N} + \mathrm{OH} \rightleftharpoons \mathrm{H} + \mathrm{NO}$ is the most dominant reaction for miscanthus NO production. It is worth noting that in the particle group configuration, the dense particle group leads to O_2 deficiency in the vicinity of the particles. Therefore, in the particle group configuration, this O_2 deficiency deactivates the direct reactions with O_2 towards NO formation. As a result, the pathways, including the available radicals around the flame, such as OH, become more dominant. Since in the particle group configuration, NO_x emission can change based on the local thermo-chemical conditions, to understand the origin of different pathways in particle group configuration in comparison with single-particle configuration, the flame topology and the local NO_x emissions should be investigated. In the next section, these interactions are discussed in more detail.

12.5.5 Flame Topology Effects on NO_x Formation

After investigating the global NO_x formation pathways in particle groups in comparison with the single-particle configuration, the interactions between the local thermo-chemical conditions and NO_x formation is studied. To this end, the same torrefied miscanthus particle group configuration as discussed in Sect. 12.5.4 is considered. Figure 12.17 depicts the opening flame topology at the statistically steady state in the dense particle group configuration, which is illustrated with the OH mole fraction alongside the local NO_x mole fraction in the numerical domain. The local comparison with the flame topology and the NO_x emissions shows that both local maxima of NO_x and OH mole fractions occurs around stoichiometric mixtures.

Interestingly the global maximum of NO_x is observed at the flame tip in the particle stream centre. At this location the nitrogen-containing volatile release has ended and due to high local gas temperature in the vicinity of small radicals shown in Fig. 12.16 the NO_x production is accelerated.

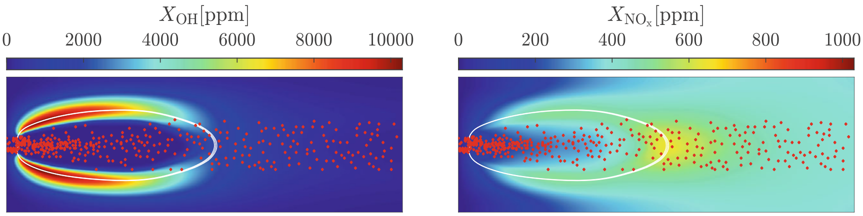

Fig. 12.17 Snapshots of the OH and NO_x mole fractions in a miscanthus flame at a time with statistically steady-state conditions ($t = 330$ ms). Particles are visualised with red points, and the stoichiometric mixture fraction $Z_{st} \approx 0.15$ is visualised with white isolines

In Fig. 12.18a), a clear demonstration of this behaviour is presented by showing the distribution of X_{NO_x} and the source terms for N-containing volatiles and NO_x in mixture fraction space coloured by OH mole fraction. The joint correlations with respect to X_{OH} shows two distinct peaks for the X_{NO_x} at $Z = Z_{st}$. By comparing these peaks with the flame topology depicted in Fig. 12.17, it can be concluded that these peaks are related to the high OH region at the flame location and the low OH region at the particle stream centre. As observed in Fig. 12.17, the peak related to the low OH region is the global maximum of NO_x. Although the local maximum of the NO_x occurs around stoichiometry, high NO_x mole fractions can also be observed in rich areas. As observed in Fig. 12.18b), the highest production rate of NO_x ($\dot{\omega}_{NO_x}$), occur in the rich region, which is in the vicinity of the particle stream itself.

The joint correlations with respect to X_{OH} shows two distinct peaks for the X_{NO_x} at $Z = Z_{st}$. By comparing these peaks with the flame topology depicted in Fig. 12.17, it can be concluded that these peaks are related to the high OH region at the flame location and the low OH region at the particle stream centre. As observed in Fig. 12.17, the peak related to the low OH region is the global maximum of NO_x. Although the local maximum of the NO_x occurs around stoichiometry, high NO_x mole fractions can also be observed in rich areas. As observed in Fig. 12.18b), the highest production rate of NO_x ($\dot{\omega}_{NO_x}$), occur in the rich region, which is in the vicinity of the particle stream itself. This observation underlines the importance of fuel-NO_x

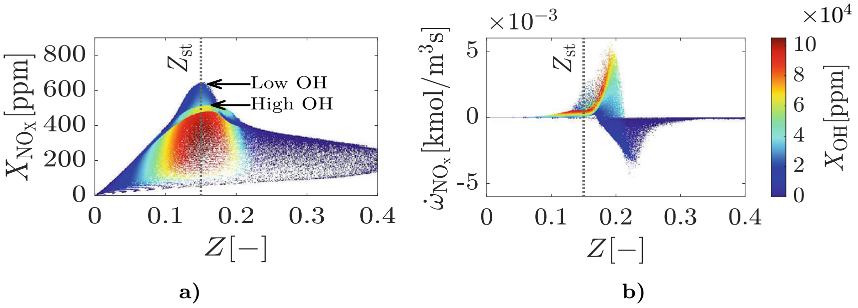

Fig. 12.18 **a)** NO_x mole fraction (X_{NO_x}), and **b)** NO_x chemical source term ($\dot{\omega}_{NO_x}$) of the selected torrefied miscanthus flame in mixture fraction space coloured by OH mole fraction

pathways in the overall NO_x formation, which is consistent with previous findings for coal combustion [25].

12.5.6 Effect of Operating Conditions on NO_x Formation

Furnace operating conditions can significantly influence NO_x emissions from the combustion of solid pulverised fuels [27]. Examining the effects of various operating conditions on NO_x formation pathways can improve the understanding of NO_x sensitivity to different parameters. Therefore, after investigating the NO_x formation pathways for a reference biomass flame, a parametric study is performed to investigate the sensitivity of NO_x formation with respect to different operating conditions. In Sect. 12.5.1, the effect of furnace temperature on the NO_x emissions was presented. In this section, the effect of atmospheric composition on the NO_x formation is investigated.

To evaluate the atmosphere effects, air and oxy-fuel atmospheres with 21% O_2 are considered. Also, the effect of changing oxygen concentration in the oxidiser by increasing the O_2 content by 10% (31% O_2) is studied. Particle group simulations with the torrefied miscanthus in the DTF configuration were performed. Figure 12.19a) shows the flame illustrated with the OH mole fraction. Lower OH intensity can be observed in oxy-fuel atmosphere, which originates from the higher heat capacity of CO_2 compared to N_2 and different reaction pathways in O_2/CO_2 atmosphere in comparison with O_2/N_2 [22].

In an oxygen-rich atmosphere, more H radicals are consumed through the reaction $CO_2 + H \rightarrow CO + OH$, which significantly impacts the overall radical pool. Depletion of H radicals significantly impacts the reaction $O_2 + H \rightarrow OH + O$, the most important chain branching reaction for ignition and combustion. This results in a weaker flame and lower reactivity and, thus, less NO_x formation in oxy-fuel atmosphere as shown in Fig. 12.19b). It is worth noting that increasing the oxygen content in different

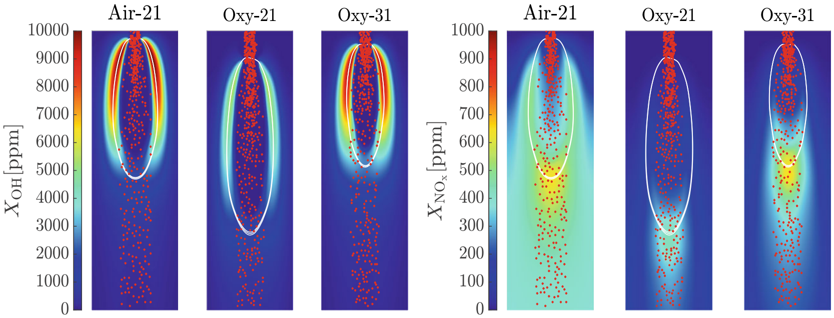

a) OH mole fraction **b)** NO_x mole fraction

Fig. 12.19 Effect of different atmospheric compositions on **a)** flame topology visualised by OH mole fraction and **b)** NO_x mole fraction at the time with statistically steady-state

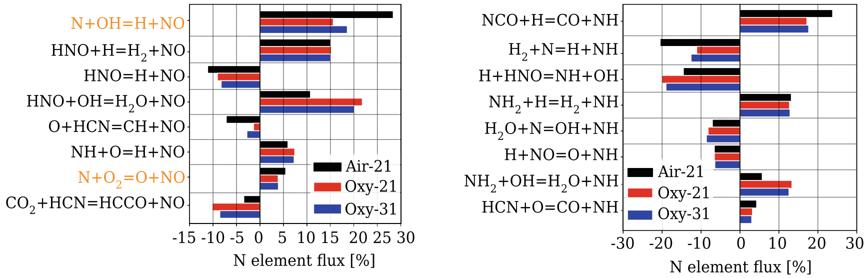

a) ROPA of NO **b)** ROPA of NH

Fig. 12.20 Effect of different atmospheres in ROPA of **a)** NO and **b)** NH, averaged over the entire computational domain and simulation time. The extended Zeldovich reactions are coloured orange

atmospheres increases the reactivity, and, as a result, a higher amount of NO_x values can be observed in those conditions.

To gain a deeper understanding of the effect of atmospheric composition on the NO_x formation mechanism, the rate of production analysis (ROPA) of NO at different atmospheres is compared in Fig. 12.20a). Comparing the rate of production of NO shows that, unlike in air, the HNO pathways in the oxy-fuel atmosphere become more important than N pathways, and $HNO + OH \rightleftharpoons H_2O + NO$ becomes the most important reaction for NO production.

As mentioned in Sect. 12.5.3, direct N-containing radicals such as N and HNO originate from the NH radical. To this end, the rate of production of NH can provide a deeper understanding of the main pathways towards NO production under different atmospheres. Figure 12.20b) highlights the differences in NH production under different atmospheres. It can be observed that in the oxy-fuel atmosphere, a higher NH consumption rate for the reaction $NH + OH \rightleftharpoons H + HNO$ and lower NH consumption rate for reaction $NH + H \rightleftharpoons H2 + N$ is the leading cause for higher direct production of NO from HNO radical in oxy-fuel atmosphere. It is worth noting that increasing oxygen concentration increases the consumption rate of all nitrogen-containing radicals, which results in higher NO production compared to the lower oxygen concentration case in the same atmosphere.

12.6 Conclusion

In this chapter, ignition, combustion, and pollutant formation pathways of coal and biomass particles were numerically studied in different configurations and under different conditions. Numerical results were analysed to understand the interactions between particles, flow and chemistry and to explain the ignition, combustion, and pollutant formation pathways of solid fuel particles under different operating conditions. Detailed simulations and discussions for modelling ignition and combustion of single particle and particle groups in laminar conditions are provided in Sect. 12.3, in which, at first, the ignition and combustion of single coal and walnut shells were compared. The observations showed similar combustion characteristics in coal and biomass due to the cancellation of competing effects of particle mass and moisture content. Observations showed that the flame structure is sensitive to different operating conditions, such as particle size and O_2 content, and the flame distance is directly related to the competition between O_2 diffusion rate and the volatile release rate.

The investigation of the effects of particle/particle interactions on the ignition and flame topology of solid fuels using different particle group configurations shows that increasing the particle number density leads to a delay in the ignition time because of the oxygen deficiency and energy sink due to particle heat-up. This leads to the opening flame behaviour in the co-flow laminar particle jet flames. The simulations employing detailed kinetics for solid and gas phase provide a baseline for assessing the reduced-order models used in large-scale simulations. Therefore, the simplified assumptions in the tabulated flamelet models and the simplified solid kinetic models were compared with the detailed simulations. It was found that well fitted reduced-order solid kinetic models based on the detailed models can predict the particle behaviour correctly. In addition, since the particle/chemistry interactions are neglected in the flamelet tables, these models mispredict the quantities of interest near the particles outside the flammability limit.

In Sect. 12.4, the effect of particle clustering in a particle group configuration on the ignition and combustion of solid fuels under homogeneous isotropic turbulence conditions was studied. It was shown that ignition is more likely to occur outside of particle clusters, where more suitable thermo-chemical conditions for ignition exist. Also, after forming the first auto-ignited regions, the growth and merging of individual ignited regions are the primary mechanisms for flame propagation. Afterwards, the DNS dataset was used to assess the FPV model using the error decomposition and optimal estimator concept. The analyses showed that mixture fraction, progress variable, and enthalpy are the best set of input parameters for the flamelet table. Neglecting the effects of enthalpy and heat loss increases the total modelling errors. In addition, the definition of the input parameters, such as the progress variable, was found to impact the model performance significantly. The analysed reduced order models are utilised for large-scale burner simulations in Chap. 19.

In Sect. 12.5, the NO_x formation during the ignition and combustion of biomass particles under laminar conditions was analysed. Solid miscanthus particles, as a biomass fuel, were employed in a drop tube configuration to study the NO_x formation pathways. Coal and biomass showed similar type of direct nitrogen-containing radicals of N, NH, and HNO for NO formation. However, due to different volatile chemical compositions, completely different reaction pathways in coal and biomass were observed. Additionally, particle/particle interactions were investigated and O_2

deficiency was found to be the leading cause of different pathways between single-particle and particle group combustion. In the particle group combustion, the local maximum of NO_x occurs around stoichiometric conditions, and the total maximum of NO_x occurs at the flame tip in the particle stream centre around $Z = Z_{st}$ towards the rich region. In addition, the reaction pathways analysis showed that the main NO_x formation contributors are the fuel-NO_x pathways, and the largest share of NO_x destruction is through the reburn mechanism. Finally, it was also observed that operating conditions such as oxidiser composition significantly changes the NO_x formation pathways and oxy-fuel condition and lower O_2 content lead to lower NO_x production.

Acknowledgements This work has been funded by the Deutsche Forschungsgemeinschaft (DFG, German Research Foundation)-—215035359-—SFB/TRR 129 'Oxyflame'.

References

1. Attili, A., Bisetti, F., Mueller, M. E. and Pitsch, H. "Effects of Non-Unity Lewis Number of Gas-Phase Species in Turbulent Nonpremixed Sooting Flames". *Combustion and Flame* 166 (2016), 192–202. https://doi.org/10.1016/j.combustflame.2016.01.018
2. Farazi, S., Hinrichs, J., Davidovic, M., Falkenstein, T., Bode, M., Kang, S., Attili, A. and Pitsch, H. "Numerical Investigation of Coal Particle Stream Ignition in Oxy-Atmosphere". *Fuel* 241 (2019), 477–487. https://doi.org/10.1016/j.fuel.2018.11.108
3. Cai, L., Kruse, S., Felsmann, D. and Pitsch, H. "A Methane Mechanism for Oxy-Fuel Combustion: Extinction Experiments, Model Validation, and Kinetic Analysis". *Flow, Turbulence and Combustion* 106.2 (2021), 499–514. https://doi.org/10.1007/s10494-020-00138-w
4. Miller, R. S. and Bellan, J. "Direct Numerical Simulation of a Confined Three-Dimensional Gas Mixing Layer with One Evaporating Hydrocarbon-Droplet-Laden Stream". *Journal of Fluid Mechanics* 384 (1999), 293–338. https://doi.org/10.1017/S0022112098004042
5. Farazi, S., Attili, A., Kang, S. and Pitsch, H. "Numerical Study of Coal Particle Ignition in Air and Oxy-Atmosphere". *Proceedings of the Combustion Institute* 37.3 (2019), 2867–2874. https://doi.org/10.1016/j.proci.2018.07.002
6. Li, T., Farmand, P., Chen, H., Boehme, C., Nicolai, H., Hasse, C., Pitsch, H. and Böhm, B. "Homogeneous Ignition and Volatile Flame Structure of Single Bituminous Coal and Walnut Shell Particles: Effects of Particle Size and Gas Atmosphere". *Fuel* 371 (2024), 131955. https://doi.org/10.1016/j.fuel.2024.131955
7. Li, T., Farmand, P., Geschwindner, C., Greifenstein, M., Köser, J., Schumann, C., Attili, A., Pitsch, H., Dreizler, A. and Böhm, B. "Homogeneous Ignition and Volatile Combustion of Single Solid Fuel Particles in Air and Oxy-Fuel Conditions". *Fuel* 291 (2021). https://doi.org/10.1016/j.fuel.2020.120101
8. Li, T., Geschwindner, C., Köser, J., Schiemann, M., Dreizler, A. and Böhm, B. "Investigation of the Transition from Single to Group Coal Particle Combustion Using High-Speed Scanning OH-LIF and Diffuse Backlight-Illumination". *Proceedings of the Combustion Institute* 38 (2021), 4101–4109. https://doi.org/10.1016/j.proci.2020.06.314
9. Farmand, P., Nicolai, H., Schumann, C., Attili, A., Berger, L., Li, T., Geschwindner, C., di Mare, F., Hasse, C., Böhm, B., Janicka, J. and Pitsch, H. "Numerical Investigation and Assessment of Flamelet-Based Models for the Prediction of Pulverized Solid Fuel Homogeneous Ignition and Combustion". *Combustion and Flame* 235 (2022), 111693. https://doi.org/10.1016/j.combustflame.2021.111693
10. Attili, A., Farmand, P., Schumann, C., Farazi, S., Böhm, B., Li, T., Geschwindner, C., Köser, J., Dreizler, A. and Pitsch, H. "Numerical Simulations and Experiments of Ignition of Solid

Particles in a Laminar Burner: Effects of Slip Velocity and Particle Swelling". *Flow, Turbulence and Combustion* 106 (2020), 515–531. https://doi.org/10.1007/s10494-020-00222-1

11. Li, T., Schiemann, M., Köser, J., Dreizler, A. and Böhm, B. "Experimental Investigations of Single Particle and Particle Group Combustion in a Laminar Flow Reactor Using Simultaneous Volumetric OH-LIF Imaging and Diffuse Backlight-Illumination". *Renewable and Sustainable Energy Reviews* 136 (2021), 110377. https://doi.org/10.1016/j.rser.2020.110377
12. Palmore, J. A. and Desjardins, O. "Technique for Forcing High Reynolds Number Isotropic Turbulence in Physical Space". *Physical Review Fluids* 3.3 (2018). https://doi.org/10.1103/PhysRevFluids.3.034605
13. Farmand, P., Nicolai, H., Usman, M., Berger, L., Attili, A., Gauding, M., Hasse, C. and Pitsch, H. "Modeling homogeneous ignition processes of clustering solid particle clouds in isotropic turbulence". *Fuel*, Elsevier 371 (2024), 132054. https://doi.org/10.1016/j.fuel.2024.132054
14. Lau, T. C. W. and Nathan, G. J. "The Influence of Stokes Number on Particle Clustering within a Two-Phase Turbulent Jet". *7^{th} Australian Conference on Laser Diagnostics in Fluid Mechanics and Combustion*. Melbourne, Australia, 2015.
15. Nicolai, H., Debiagi, P., Wen, X., Dressler, L., Maßmeyer, A., Janicka, J. and Hasse, C. "Flamelet LES of Swirl-Stabilized Oxy-Fuel Flames Using Directly Coupled Multi-Step Solid Fuel Kinetics". *Combustion and Flame* 241 (2022), 112062. https://doi.org/10.1016/j.combustflame.2022.112062
16. Rieth, M., Clements, A. G., Rabaçal, M., Proch, F., Stein, O. T. and Kempf, A. M. "Flamelet LES Modeling of Coal Combustion with Detailed Devolatilization by Directly Coupled CPD". *Proceedings of the Combustion Institute* 36.2 (2017), 2181–2189. https://doi.org/10.1016/j.proci.2016.06.077
17. Nicolai, H., Li, T., Geschwindner, C., di Mare, F., Hasse, C., Böhm, B. and Janicka, J. "Numerical Investigation of Pulverized Coal Particle Group Combustion Using Tabulated Chemistry". *Proceedings of the Combustion Institute* 38.3 (2021), 4033–4041. https://doi.org/10.1016/j.proci.2020.06.081
18. Monchaux, R., Bourgoin, M. and Cartellier, A. "Analyzing Preferential Concentration and Clustering of Inertial Particles in Turbulence". *International Journal of Multiphase Flow* 40 (2012), 1–18. https://doi.org/10.1016/j.ijmultiphaseflow.2011.12.001
19. Wen, X., Rieth, M., Han, W., Chen, J. H. and Hasse, C. "Investigation of the Ignition Processes of a Multi-Injection Flame in a Diesel Engine Environment Using the Flamelet Model". *Proceedings of the Combustion Institute* 38.4 (2021), 5605–5613. https://doi.org/10.1016/j.proci.2020.05.057
20. Krüger, J., Haugen, N. E., Mitra, D. and Løvås, T. "The Effect of Turbulent Clustering on Particle Reactivity". *Proceedings of the Combustion Institute* 36.2 (2017), 2333–2340. https://doi.org/10.1016/j.proci.2016.06.187
21. Berger, L., Kleinheinz, K., Attili, A., Bisetti, F., Pitsch, H. and Mueller, M. E. "Numerically Accurate Computational Techniques for Optimal Estimator Analyses of Multi-Parameter Models". *Combustion Theory and Modelling* 22.3 (2018), 480–504. https://doi.org/10.1080/13647830.2018.1424353
22. Farmand, P., Boehme, C., Steffens, P., Nicolai, H., Loffredo, F., Debiagi, P., Girhe, S., Chu, H., Gauding, M., and Hasse, C.,"Numerical investigation and modeling of NOx formation in pulverized biomass flames under air and oxyfuel conditions". *Combustion and Flame*. Elsevier 279 (2025) 114284. https://doi.org/10.1016/j.combustflame.2025.114284
23. Ren, X., Sun, R., Meng, X., Vorobiev, N., Schiemann, M. and Levendis, Y. A. "Carbon, Sulfur and Nitrogen Oxide Emissions from Combustion of Pulverized Raw and Torrefied Biomass". *Fuel* 188 (2017), 310–323. https://doi.org/10.1016/j.fuel.2016.10.017
24. Panahi, A., Sirumalla, S. K., West, R. H. and Levendis, Y. A. "Temperature and Oxygen Partial Pressure Dependencies of the Coal-Bound Nitrogen to NO_x Conversion in O_2/CO_2 Environments". *Combustion and Flame* 206 (2019), 98–111. https://doi.org/10.1016/j.combustflame.2019.04.015
25. Shamooni, A., Debiagi, P., Wang, B., Luu, T. D., Stein, O. T., Kronenburg, A., Bagheri, G., Stagni, A., Frassoldati, A., Faravelli, T., Kempf, A. M., Wen, X. and Hasse, C. "Carrier-Phase

DNS of Detailed NO_x Formation in Early-Stage Pulverized Coal Combustion with Fuel-Bound Nitrogen". *Fuel* 291 (2021). https://doi.org/10.1016/j.fuel.2020.119998

26. Androulakis, I. P., Grenda, J. M. and Bozzelli, J. W. "Time–Integrated Pointers for Enabling the Analysis of Detailed Reaction Mechanisms". *AIChE Journal* 50.11 (2004), 2956–2970. https://doi.org/10.1002/aic.10263
27. Shamooni, A., Stein, O. T., Kronenburg, A., Kempf, A. M., Debiagi, P., Li, T., Dreizler, A., Böhm, B. and Hasse, C. "Fully-Resolved Simulations of Volatile Combustion and NO_x Formation from Single Coal Particles in Recycled Flue Gas Environments". *Proceedings of the Combustion Institute* 39.4 (2023), 4529–4539. https://doi.org/10.1016/j.proci.2022.07.034